Aeroacoustic Noise Prediction of a Wing with a Droop-nose Leading Edge

Seiji Adachi, Peter Brandstätt and John C. Simpson

Fraunhofer Institute for Building Physics, 70569 Stuttgart, Germany, Email: seiji.adachi@ibp.fraunhofer.de

Introduction

In the EU Clean Sky Green Regional Aircraft project, we are proposing a 3D wing model equipped with a gapless leading-edge inclined downward, i.e., droop-nose, as a possible solution for reducing aeroacoustic noise. The droop-nose leading-edge device is generally considered to be quieter than the traditional leading-edge slat, because the gap between the wing and the slat, at which a turbulent flow may occur, does not exist. We have already designed a few possible droop-nose wing models. The purpose of this research is to estimate both the aerodynamic and aeroacoustic performance of these models numerically. The high-lift baseline that has a trailing flap but has no droop-nose leading-edges is also analyzed for comparison. Due to limitation of space, this paper presents the results of the baseline and of two droop-nose wing models only. The model showing the best performance will be examined further in wind tunnel tests.

CFD Analysis

Wing models

The droop-nose wing models to be analyzed are all based on the baseline wing of a geared turbo fan aircraft in the high-lift condition, where the trailing flaps are deployed. Although this original wing has a winglet, it has been removed for the analysis. This is because the results of the analysis will be compared with those of wind tunnel tests that will be performed without the winglet. The fuselage is also omitted in the same reason.

Figure 1 shows four different models analyzed here:

(a) the original clean wing,
(b) the high-lift baseline (HL-BL) that has the deployed tailing flap but has no leading-edge devices,
(c) the high-lift skewed droop configuration (HL-SD) that has the same trailing flap as HL-BL and has a leading-edge whose droop angle is decreased linearly from 15 degree at the 18 % span to 0 degree at the 98 % span,
(d) the high-lift constant droop (HL-CD) configuration that has a leading-edge whose droop angle is fixed to 15 degree along the entire span (i.e., 18 to 98 % span).

Conditions and CFD mesh

Stationary flow simulation has been carried out by solving the incompressible Navier-Stokes equations with a renormalization group k-ϵ turbulence model[1]. For analyzing the clean wing, a cruising condition of Mach = 0.74 and Re/L = $5.8 \times 10^6\,\mathrm{m}^{-1}$ was assumed. For the other high-lift configurations, a landing condition of Mach = 0.21 and Re/L = $4.1 \times 10^6\,\mathrm{m}^{-1}$ was assumed.

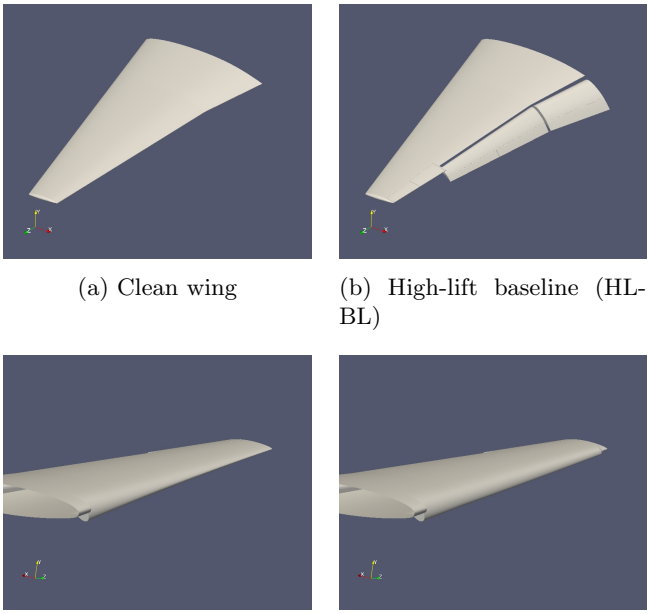

(a) Clean wing (b) High-lift baseline (HL-BL)

(c) High-lift skewed droop (HL-SD) (d) High-lift constant droop (HL-CD)

Figure 1: Analyzed wing models

Each model is placed in a computational domain of 80 (longitudinal) × 80 (vertical) × 40 (lateral) m^3 size. The root of the wing is attached to an 80 × 80 m^2 wall. A hex-dominant mesh with eight-step refinement toward the wing has been generated in the domain. Seven layers are placed on the surface of the wing. The number of the cells becomes about 15.2 millions. On the wall where the wing is attached, a slip boundary condition is assumed. On the other boundary surfaces, a constant flow velocity of 219.44 m/s (Mach = 0.74) in the case of the clean wing and of 70 m/s (Mach = 0.21) in the case of the high-lift configurations is assumed. In the analysis, $y+$ has been confirmed to be less than 300 on the entire wing surface except for a few small parts such as the trailing edge and the side walls which are not covered by the boundary layers due to geometric discontinuity.

Lift and drag coefficients

Figure 2 shows calculated lift and drag coefficients: c_l and c_d. Those of the clean wing, HL-BL, HL-SD, and HL-CD configurations are depicted in blue, green, red and light blue lines, respectively. The c_l of the clean wing is gradually increasing along with the angle of attack α. At 16 degree, c_l takes its maximum of 1.56 and then falls off with a further increase in α due to a stall. The high-lift configurations have larger c_l overall. In the

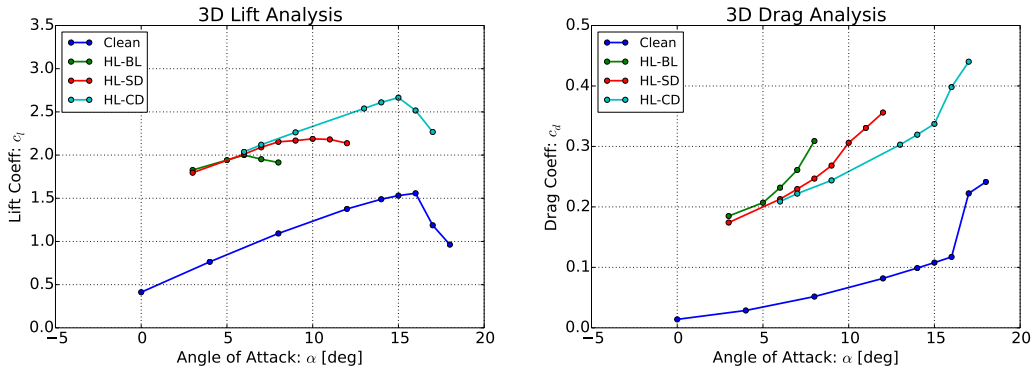

Figure 2: Calculated lift (left) and drag (right) coefficients

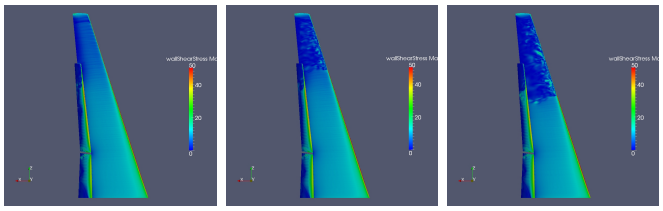

$\alpha = 5$ deg. $\alpha = 6$ deg. $\alpha = 7$ deg.

Figure 3: Flow separation characteristics of the HL-BL configuration.

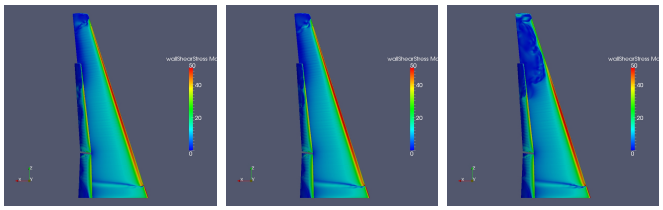

$\alpha = 14$ deg. $\alpha = 15$ deg. $\alpha = 16$ deg.

Figure 4: Flow separation characteristics of the HL-CD configuration.

HL-BL configuration, c_l is increased up to 2.0 at $\alpha = 6$ degree. This increase can be extended in the droop-nose configurations. This effect is, however, limited in the HL-SD configuration where $c_l^{max} = 2.19$ at $\alpha = 10$ degree is observed. Better performance can be obtained in the HL-CD configuration: $c_l^{max} = 2.66$ at 15 degree. In the c_d plots, similar stall behavior can be observed commonly in all the configurations. These c_d curves are increased gradually along with α at first. They are then increased suddenly after α exceeds the stall angles. As far as the aerodynamic properties are concerned, the HL-CD configuration is found to be promising.

Flow separation characteristics

To examine the aerodynamic characteristics more, skin friction, or the magnitude of wall shear stress on the surface, are drawn on the suction side of the wing. Figures 3 and 4 shows the results of the HL-BL and HL-CD configurations, respectively. In the HL-BL configuration, the flow starts separating outboard at 6 degree suddenly. This explains why aerodynamic performance is not improved very much in the HL-SD configuration, which has a smaller droop angle outboard than inboard. Placing a droop-nose with a large angle outboard is more effective to prevent flow separation and thus to delay the stall. This is, in fact, realized in the HL-CD configuration. Although flow separation occurs outboard also in this configuration, the aerodynamic performance is much improved; Its stall angle is 9 degree larger than that of the HL-BL configuration. In Figure 4, one may find that flow separation has already occurred at the wing tip before stall at $\alpha = 14$ degree. This is probably due to the absence of the winglet.

CAA Analysis

Analyzed models and the angle of attack

As we have found that the HL-CD configuration is aerodynamically promising, CAA analysis of this configuration is performed in this section and sound pressure level of noise radiated from the model is estimated. For comparison, the HL-BL configuration is also analyzed.

For a neutral comparison, the analysis is performed at the angle where the maximum c_l is obtained (stall angle), which is 6 degree for the HL-BL and 15 degree for the HL-CD configurations. To confirm whether a larger noise level is actually simulated after a stall happens, the analysis was also performed at the angle one degree larger than the stall angle for each configuration.

Analysis method

The analysis is composed of three steps:

(1) Stationary flow field $\boldsymbol{U}(\boldsymbol{x})$ and turbulence quantities of kinetic energy $k(\boldsymbol{x})$ and dissipation rate $\epsilon(\boldsymbol{x})$ have already been calculated in CFD analysis. From these quantities, transient turbulent flow field $\boldsymbol{U}(\boldsymbol{x}, t)$ is reconstructed with a stochastic noise generation and radiation (SNGR) model[2, 3].

(2) According to the aeroacoustic analogy[4, 5], sound pressure in the vicinity of the wing is computed by solving inhomogeneous wave equations with a source term based on Lighthill stress tensor $T_{ij} = U_i U_j$.

(3) Kirchhoff-Helmholtz integral is finally performed over a control surface covering the wing to compute far-field sound pressure.

The details of this method are presented in [6].

Transient CAA simulation has been done for duration of 0.17 second on a hex mesh with uniform resolution generated in $13 \times 4 \times 15.8$ m^3 domain. The mesh resolution is 3.3 cm, which is fine enough to resolve sound waves up to 5 kHz. Perfect matched layers are placed on the

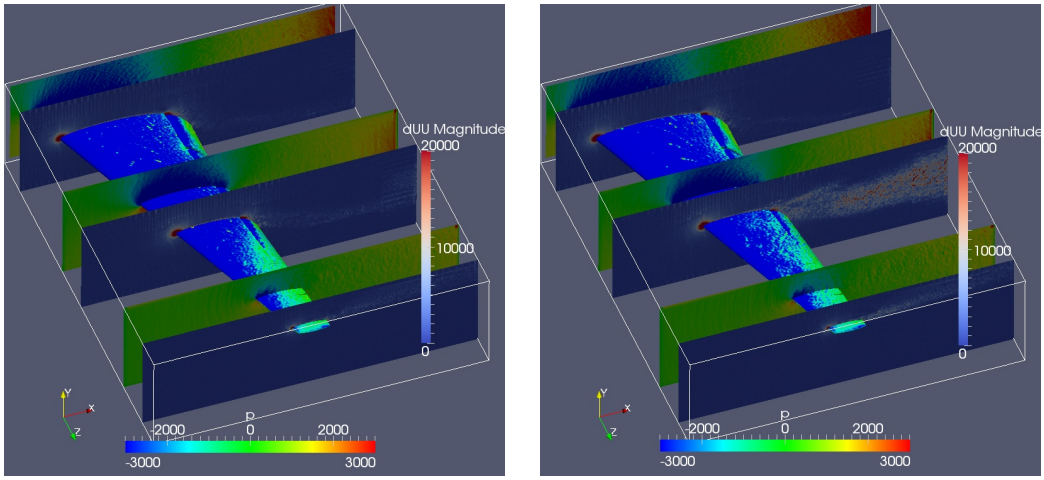

Figure 5: CAA simulation results of HL-BL: Sound source strength in blue-to-red color and pressure in RGB color map. At the stall angle ($\alpha = 6$ degree) on the left and after the stall ($\alpha = 7$ degree) on the right.

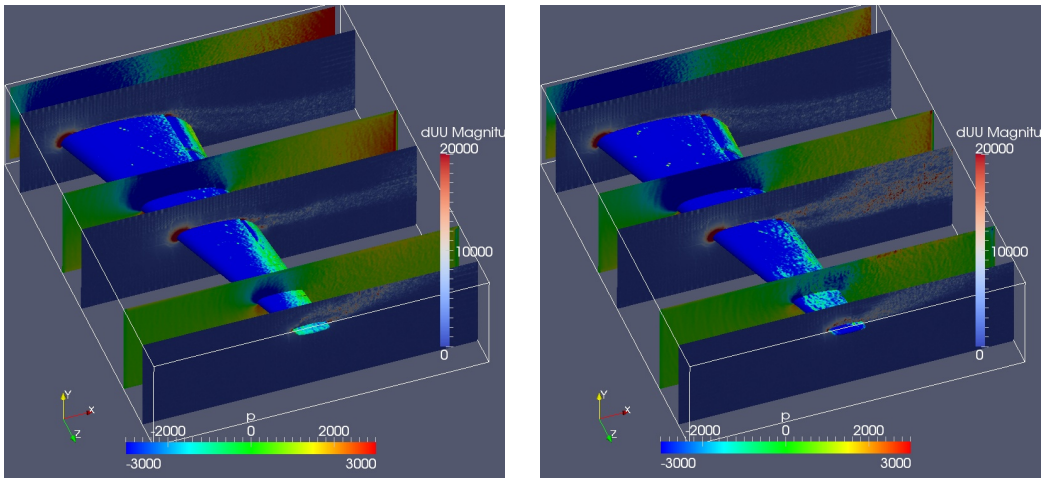

Figure 6: CAA simulation results of HL-CD: Sound source strength in blue-to-red color and pressure in RGB color map. At the stall angle ($\alpha = 15$ degree) on the left and after the stall ($\alpha = 16$ degree) on the right.

boundaries so that wave radiating from the wing is not reflected back to the computational domain. The number of cells amount to 21.8 million.

Simulation results

The source term $\partial_j U_j U_i$, or divergence of Lighthill tensor reconstructed in the SNGR model is plotted together with sound pressure radiating from the wing for the HL-BL and HL-CD configurations in Figures 5 and 6, respectively. In these figures, large magnitude of the source term is observed at the leading edge and the channel between the wing and the trailing flap. This implies that noise radiates mainly from these areas. There is also a noise source near the wing tip in the HL-CD configuration. After the stall, both configurations have an additional noise source in the wake of the flow passing mid-board over the wing. This is caused by flow separation. In the pressure distribution shown in the RGB color map, small fluctuation or propagating sound that is superimposed on the static pressure can be observed. This also implies that noise is generated near the areas of the leading edge and of the channel between the wing and the flap.

Far-field noise spectra and sound pressure levels

Figures 7 and 8 plot noise waveforms and spectra computed at positions 10 m away from the wing tip in five different downward directions for these two wing configurations. The angles of -180, -135, -90, -45 and 0 degree imply the forward, forward-downward, downward, backward-downward and backward directions, respectively. The figures show continuous spectra having a broad hump in the frequency range between 2 and 3 kHz. There are also frequency components lower than 200 Hz, which result in slow fluctuation seen in the waveforms. Both configurations have similar radiation directivity. Radiation in the forward and backward directions is larger than that in the downward direction. The overall sound pressure level is apparently higher after the stall than at the stall angle.

The A-weighted overall sound pressure level (SPL) is calculated in each direction and shown as radiation patterns in Figure 9. These indicate that larger radiation occurs in the forward and backward directions than in the upward and downward directions. This is likely due to the two main noise sources at the leading edge and at the channel between the wing and the trailing flap. The SPL averaged over all the directions in dB(A) is 126.6 at the stall angle ($\alpha = 6°$) and 128.9 after the stall ($\alpha = 7°$) for the HL-BL and 126.9 at the stall angle ($\alpha = 15°$) and 129.2 after the stall ($\alpha = 16°$) for the HL-CD configurations. There is no significant difference between the two configurations. Note here, however, that the stall angle of the HL-CD configuration is much larger than that of the HL-BL. In each configuration, the SPL increases about 2 dB when the angle of attack is one degree increased

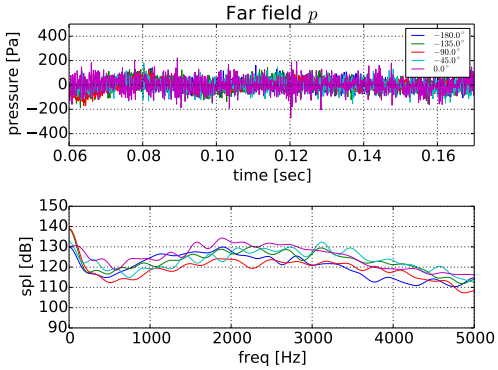

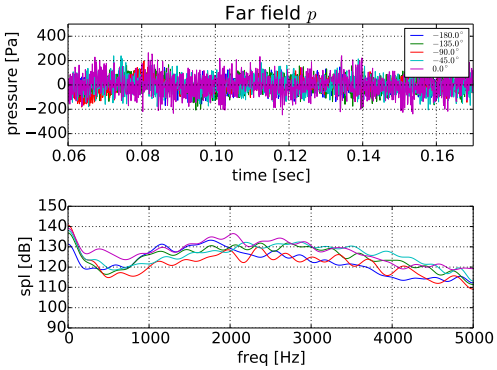

Figure 7: Far-field nose waveforms (upper) and spectra (lower) of HL-BL: At the stall angle ($\alpha = 6$ degree) on the left and after the stall ($\alpha = 7$ degree) on the right.

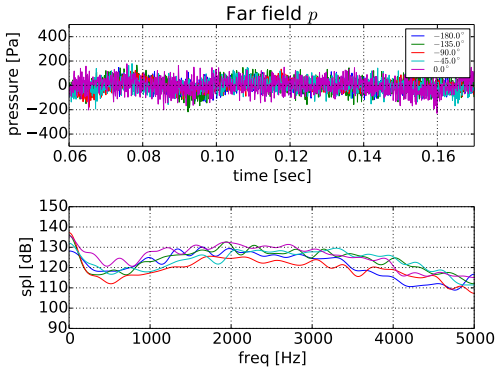

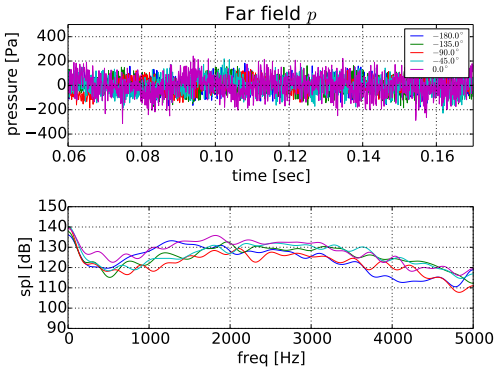

Figure 8: Far-field nose waveforms (upper) and spectra (lower) of HL-CD: At the stall angle ($\alpha = 15$ degree) on the left and after the stall ($\alpha = 16$ degree) on the right.

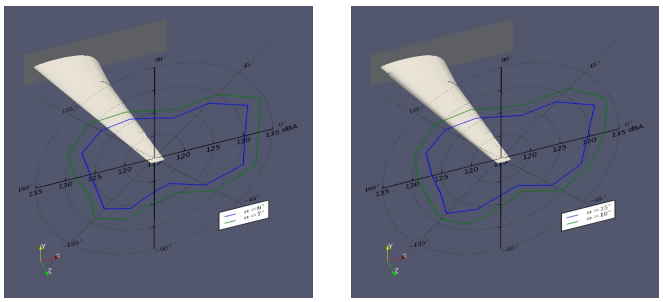

Figure 9: A-weighted overall SPL in different directions: The HL-BL (left) and HL-CD (right) configurations.

from its stall angle. This is a reasonable result because an extra noise source due to the turbulent wake behind the wing appears after the stall.

Summary

Wing models with full-span droop-nose leading-edge devices were numerically examined. In CFD analysis, the model having a constant droop angle was shown to have a better performance. In CAA analysis, this droop-nose model was further examined in comparison with the high-lift baseline, which has a deployed trailing flap but no leading-edge devices. It was found that the same noise level is estimated for both the baseline and droop-nose configurations at their stall angles, although the droop-nose configuration has the stall angle 9 degree larger than that of the baseline. In each configuration, the SPL increases about 2 dB when a stall occurs. This implies that the CAA analysis adequately captures increase in turbulence and noise after a stall.

Acknowledgments

This research is funded by the European Commission in the Seventh Framework Programme (FP7/2007-2013) for the Clean Sky Joint Technology Initiative under the grant agreement No. CSJU-GAM-GRA-2008-001.

References

[1] V. Yakhot, S.A. Orszag, S. Thangam, R.B. Gatski and C.G. Speziale, "Development of turbulence models for shear flows by a double expansion technique", Physics of Fluids A, **4**(7), pp. 1510–1520 (1992).

[2] C. Baily, P. Lafon and S. Candel, "A stochastic approach to compute noise generation and radiation of free turbulent flows," AIAA paper 95-092-1-6 pp. 669–674 (1995).

[3] M. Mesbah, "Flow noise prediction using the stochastic noise generation and radiation approach," Ph.D thesis Catholic University of Leuven (2006).

[4] M. J. Lighthill, "On Sound Generated Aerodynamically. I. General Theory," Proc. of the Royal Society A: Mathematical, Physical and Engineering Sciences **211**(1107) pp. 564–510 (1952).

[5] M. J. Lighthill, "On Sound Generated Aerodynamically. II. Turbulence as a Source of Sound," Proc. of the Royal Society A: Mathematical, Physical and Engineering Sciences **212**(1148) pp. 1–32 (1954).

[6] S. Adachi, P. Brandstätt, W. Herget, P. Leistner, V. Landersheim, D. Weber and J. Mueller-Roemer, "Wind Tunnel Test and CFD/CAA Analysis on a Scaled Model of a Nose Landing Gear," Proc. of Greener Aviation 2014, S2-NR-19 (2014).